


Two-dimensional strain-mapping by electron backscatter diffraction and confocal Raman spectroscopy

Cite as: J. Appl. Phys. **122**, 205101 (2017); <https://doi.org/10.1063/1.5001270>

Submitted: 23 August 2017 . Accepted: 08 November 2017 . Published Online: 27 November 2017

Andrew J. Gayle, Lawrence H. Friedman , Ryan Beams, Brian G. Bush, Yvonne B. Gerbig, Chris A. Michaels , Mark D. Vaudin, and Robert F. Cook 



View Online



Export Citation



CrossMark

ARTICLES YOU MAY BE INTERESTED IN

[Stress management on underlying GaN-based epitaxial films: A new vision for achieving high-performance LEDs on Si substrates](#)

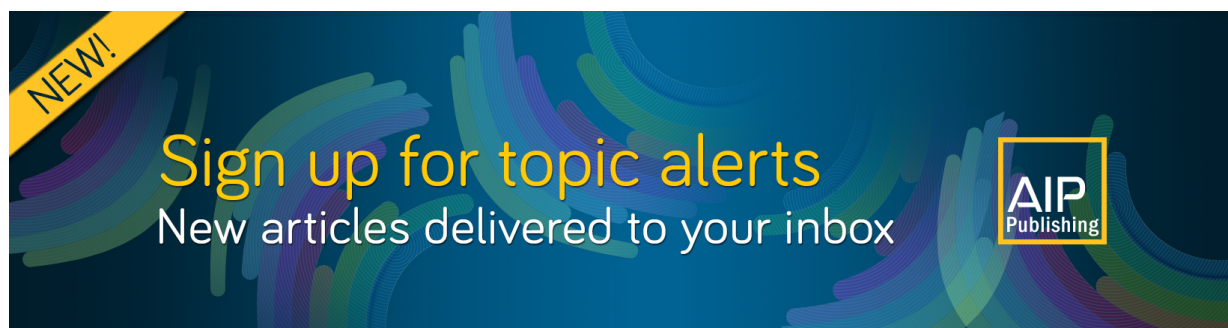
Journal of Applied Physics **122**, 204503 (2017); <https://doi.org/10.1063/1.4993985>

[Determination of transport properties in optoelectronic devices by time-resolved fluorescence imaging](#)

Journal of Applied Physics **122**, 203102 (2017); <https://doi.org/10.1063/1.5005164>

[An analysis of PN junctions in piezoelectric semiconductors](#)

Journal of Applied Physics **122**, 204502 (2017); <https://doi.org/10.1063/1.4996754>



Two-dimensional strain-mapping by electron backscatter diffraction and confocal Raman spectroscopy

Andrew J. Gayle, Lawrence H. Friedman, Ryan Beams, Brian G. Bush, Yvonne B. Gerbig, Chris A. Michaels, Mark D. Vaudin, and Robert F. Cook

Materials Measurement Science Division, National Institute of Standards and Technology, Gaithersburg, Maryland 20899, USA

(Received 23 August 2017; accepted 8 November 2017; published online 27 November 2017)

The strain field surrounding a spherical indentation in silicon is mapped in two dimensions (2-D) using electron backscatter diffraction (EBSD) cross-correlation and confocal Raman spectroscopy techniques. The 200 mN indentation created a 4 μm diameter residual contact impression in the silicon (001) surface. Maps about 50 $\mu\text{m} \times 50 \mu\text{m}$ area with 128 pixels \times 128 pixels were generated in several hours, extending, by comparison, assessment of the accuracy of both techniques to mapping multiaxial strain states in 2-D. EBSD measurements showed a residual strain field dominated by in-surface normal and shear strains, with alternating tensile and compressive lobes extending about three to four indentation diameters from the contact and exhibiting two-fold symmetry. Raman measurements showed a residual Raman shift field, dominated by positive shifts, also extending about three to four indentation diameters from the contact but exhibiting four-fold symmetry. The 2-D EBSD results, in combination with a mechanical-spectroscopic analysis, were used to successfully predict the 2-D Raman shift map in scale, symmetry, and shift magnitude. Both techniques should be useful in enhancing the reliability of microelectromechanical systems (MEMS) through identification of the 2-D strain fields in MEMS devices.

<https://doi.org/10.1063/1.5001270>

I. INTRODUCTION

As discussed in a recent review,¹ the mechanical reliability of small-scale silicon (Si) components, such as those in microelectromechanical systems (MEMS), can be enhanced by controlling either the strength of such components, largely by choice of fabrication method, or the stress or strain applied to such components during operation, by choice of component size, shape, and allowed load or deformation. The review concentrated on the former and concluded that the *strength* of Si at small scales was well understood experimentally and analytically. However, the review also noted the diversity of stress and strain states (e.g., tension, compression, bending, and torsion) experienced by MEMS components during strength tests and device operation, and it is the experimental determination of *strain* at small scales in Si that is the focus of the work here. In particular, the work describes the application and correlation of two strain measurement techniques that have appropriate spatial and strain resolutions for MEMS reliability applications—confocal Raman microscopy and electron backscatter diffraction (EBSD)—to a test vehicle with a well-defined multiaxial deformation state—a spherical indentation in a Si surface. The goal is to assess the applicability of extending the techniques from the largely one-dimensional (1-D), uniaxial fields previously examined to a two-dimensional (2-D), general biaxial field more representative of those encountered in MEMS components.

Previous Raman and EBSD stress and strain measurements often used surface-localized, 1-D line scans perpendicular to the lengths of long, narrow structures in or on the surface. The state of deformation in these measurements is

particularly simple as the perpendicular constraints of plane stress (traction-free surface) and plane strain (normal to the length) suppress all shear-stress and -strain components, leading to simplification of measurement interpretations and quantitative comparisons. Thus, 1-D line-scan Raman measurements have been compared: with EBSD measurements for long, wedge indentations in Si surfaces;^{2,3} with finite element analyses (FEA) for encapsulated interconnection lines on Si;⁴ dielectric lines in Si;⁵ conductive through vias in Si;⁶ and tensile bars of polysilicon;⁷ and, with analytical expressions, for dielectric lines in and on Si^{8,9} and Si dies soldered to copper substrates.¹⁰ 1-D line-scan EBSD measurements have been compared: with analytical expressions for SiGe lines on Si substrates;¹¹ with FEA of bent Si beams;¹² with atomic force microscopy (AFM) measurements for wedge indentations in Si surfaces;^{3,13} with analytical expressions for long, lamellar domains in barium titanate;¹⁴ and, with X-ray diffraction measurements for SiGe lines on Si substrates.¹⁵

2-D maps of stress and strain measurements have largely been restricted to qualitative interpretations: of shifts in the Si Raman peak in terms of stress adjacent to scratches¹⁶ and indentations;^{17–20} and of EBSD rotation and strain component measurements of SiGe mesas on Si substrates.²¹ Quantitative comparisons with FEA of 1-D line scans extracted from 2-D maps have been made for Raman measurements of stress in tensile bars⁷ and for EBSD measurements of strain in SiGe mesas.²¹ An exception to these qualitative studies is the detailed and quantitative interpretation of 2-D EBSD rotation and strain measurements of the elastic deformation field surrounding a Vickers indentation in Si for comparison with a FEA model.^{22,23}

In the work here, an explicit quantitative comparison is made over 2-D maps of experimental strain measurements by Raman and EBSD adjacent to a spherical indentation. Specifically, EBSD strain measurements will be used to predict Raman shifts for direct comparison with experimental Raman measurements. The methods employ completely separate physical principles in determining strain: electron diffraction from a stationary electron density in the case of EBSD and photon scattering from phonons in the case of Raman. Application of the methods requires calibration of both in multi-axial strain fields, of which this work is a continuation into 2-D of previous work. The approach follows explicitly that used in earlier 1-D wedge indentation studies.^{2,3,13}

II. MATERIALS AND METHODS

A. Spherical indentation

The test material was a single crystal (001) Si disc, 35 mm diameter \times 3 mm thick, prepared by RCA cleaning to leave a clean (001) surface with roughness of approximately 3 nm rms. The disc contained an edge flat on a (110) plane perpendicular to the (001) surface. Indentations were formed in the (001) surface in a clean-room environment using an instrumented indenter in two stages. In the first stage, a multi-millimeter scale L-shaped array of large indentations was formed using a triangular pyramid Berkovich indenter. The long arm of the L-shaped array was aligned perpendicular to the (110) flat. In the second stage, using the large indentations in the long edge of the array as fiducial markers, square arrays of small test indentations were formed using a conospherical diamond probe of nominal 5 μm tip radius. The peak load for the test indentations was 200 mN and they were separated by 1 mm to avoid overlap of the indentation deformation fields. Loading and unloading rates were 5 mN s⁻¹. The load-displacement traces of the indentations exhibited elastic, plastic, and primary phase-transformation behavior on loading and elastic and secondary phase-transformation (the “pop-out”) on unloading, typical of Si under these indentation conditions.^{18,24,25} As noted below, the spherical test indentations were very small and very shallow. The combination of the (110) flat on the disc and the large fiducial array enabled (the non-trivial) location of the test arrays and identification of specific indentations within the test arrays for comparison imaging and measurements by scanning electron microscope (SEM), AFM, EBSD, and Raman. A single indentation is examined here, but the results are representative of the indentations in the arrays. Figure 1(a) shows a SEM image of the indentation studied here; the impression outline was almost circular and approximately 4 μm in diameter. The sample frame (coordinate system) used here in the EBSD and Raman analyses (i, j) = (1, 2, 3) was taken as ([$\bar{1}\bar{1}0$], [110], [001]) and is indicated in Fig. 1(a).

Topographic height imaging of the spherically indented arrays was conducted on a Park XE-150 atomic force microscope (Park Systems, Santa Clara, CA) with a closed loop mechanized stage that allowed for rapid screening of entire arrays to identify a particular indentation of interest. Topographic information over a 30 μm \times 30 μm area was

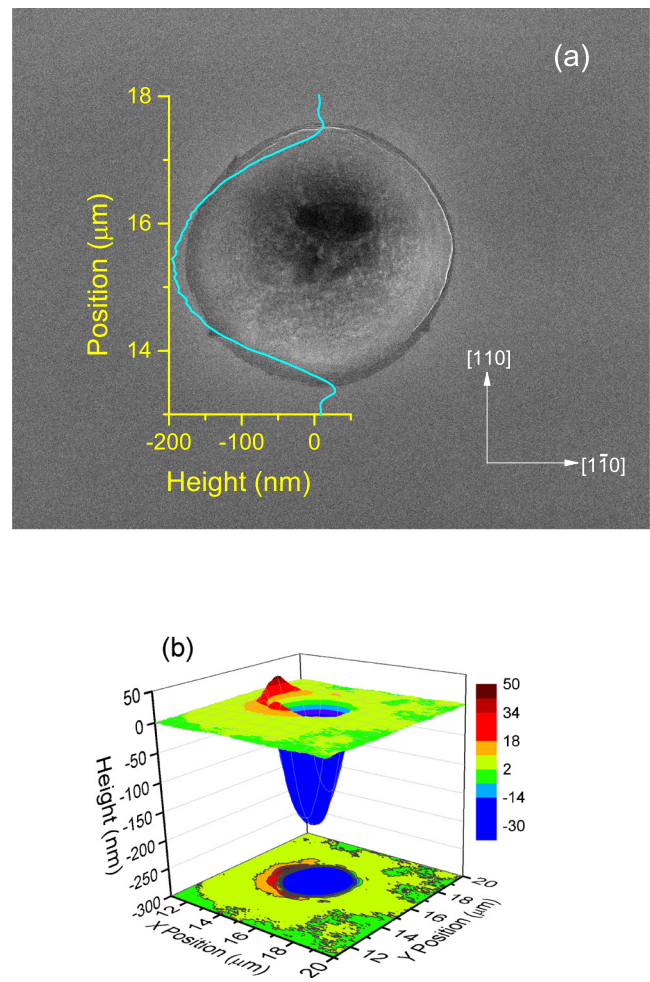


FIG. 1. (a) SEM image of the residual contact impression of a 200 mN spherical indentation in Si (5 μm radius indenter). The surface height determined by AFM is superimposed. (b) Rendered AFM height image and contour map of the residual contact impression in Si of the spherical indentation shown in (a). X and Y directions correspond to [$\bar{1}\bar{1}0$] and [110], respectively.

obtained using True Non-ContactTM imaging mode and tapping mode cantilever probes (PPP-NCHR probes, Nanosensors, Neuchâtel, Switzerland). Figure 1(b) shows clipped 9 μm \times 9 μm rendered height and color-filled contour maps centered on the indentation obtained using AFM. The final depth of the residual contact impression was about 200 nm, also shown in the superimposed center-line trace in Fig. 1(a). Large, asymmetric, and localized surface pile up, about 40 nm in height, is evident adjacent to the contact impression (the impression and pile up are most evident in the height map). Detailed SEM and AFM examination of this and other indentations from the arrays suggested that the pile up was plastically deformed material pushed sideways out of the impression and that it occurred in the same relative indentation location (e.g., left of the indentation) within a given array, indicating that the pile-ups were caused by small misalignments between the indentation column and the normal to the sample surface (exterior observations of the column suggested the misalignments were variable, but could be as much as 2°). Such misalignments are not apparent in load-displacement traces or SEM images [Fig. 1(a)] or at indentations made with much smaller loads (as previously in

Refs. 18–20). However, the AFM examination of this and other indentations from the arrays also revealed small, symmetric, distributed surface uplift, about 15 nm in height, adjacent to the impressions and decaying to the surface roughness about 10 μm from the impressions (the uplift is most evident in the contour map). Such uplift arises in elastic reaction to the plastically deformed and phase-transformed densified material pushed downwards beneath the contact impression into a localized sub-surface plastic deformation and phase-transformation zone. The localized irreversibly deformed zone of material gives rise to a residual elastic strain field in the matrix material adjacent to the zone. The uplift and residual field were the focus in prior studies of wedge indentations.^{2,3,13} The ratio of (elastic uplift/contact impression depth) for the spherical indentation here, about (15 nm/200 nm) \approx 0.08, is considerably less than that observed for the wedge indentations, about (50 nm/100 nm) \approx 0.5, suggesting that the residual strain field would be decreased in magnitude relative to that of the wedge as the irreversible deformation zone was smaller or shallower.

B. EBSD measurements

The recording and analysis of electron backscatter patterns (EBSPs) to measure strain have been described previously.^{2,3,13} Details specific to this study are provided here. The diffracted EBSPs were recorded using an Oxford-HKL system (Oxford Instruments, Abingdon, United Kingdom) installed on a JEOL 7100 SEM (JEOL USA Inc., Peabody, MA); the SEM was operated at a 20 kV accelerating voltage with a probe current of 2.3 nA and an electron spot size of \approx 2 nm. EBSPs were recorded from a square region centered on a selected indentation; the side of the square was approximately 48 μm long and EBSPs were collected over a 128×128 grid with a step size of \approx 0.373 μm . The sample was tilted at 70°. EBSPs were recorded at 0.5 s/pattern using the maximum resolution of the system: 1024 pixels \times 1344 pixels (total collection time for a grid was 2.3 h). An EBSP obtained far from the indentation impression (about 35 μm) was chosen as the reference EBSP; the other EBSPs were compared with this reference using commercial cross-correlation software (CrossCourt 3.2, BLG Productions, Bristol, United Kingdom) as follows. The EBSPs were equally cropped from both sides to 1024 \times 1024 pixels and 21 regions of interest (ROIs), 256 pixel \times 256 pixel, identically placed in each EBSP were selected. Each ROI from a strained EBSP was cross-correlated with the corresponding ROI from the reference EBSP using Fourier methods: The displacement of the peak in the cross-correlation away from the center of the ROI in a strained EBSP provided the relative shift of the diffraction pattern at the center of the ROI and was designated $q_k^{(i)}$, where (i) indicates the ROI index and k indicates a vector component. The software corrected for the movement of the EBSP pattern centers caused by scanning the electron beam over the tilted sample (“beamshift”). Over the data grid outside of the contact impression area, the mean angular error for the cross-correlated $q_k^{(i)}$ was $< 0.7 \times 10^{-4}$ (comparable to other measurements²¹) and the geometric mean over the 21 ROIs of the normalized cross-correlation function

peak heights was > 0.96 , both signifying that the data were of high quality.

The measurement of $q_k^{(i)}$ as a function of the ROI location vector, $r_k^{(i)}$, for 21 ROIs in each EBSP enabled the best-fit traceless displacement gradient tensor for the probed region, $\tilde{A}_{ij}(x, y)$, to be determined as a function of probe location $(x, y) = (x_1, x_2)$.²⁶ The full displacement gradient tensor, $A_{ij}(x, y)$, was obtained by assuming the surface to be in stress-free equilibrium such that $\sigma_{33} = 0$. Custom analysis methods were then used to subtract a 2-D linear background from the raw $A_{ij}(x, y)$ to ensure that the final $A_{ij}(x, y)$ approached zero far away from the indentation. The corrected displacement gradient tensor was then used in two ways. First, the symmetric component of A_{ij} , was calculated. In the limit of small A_{ij} (as here), this component is the infinitesimal strain, $\epsilon_{ij} = (1/2)(A_{ij} + A_{ji})$, and this calculation is a conventional use of EBSD strain mapping.^{3,22,23} Second, the Green strain tensor, $\eta_{ij} = (1/2)(A_{ij} + A_{ji} + A_{ki}A_{kj})$,^{27,28} was calculated. This tensor was required^{28–30} as an intermediate calculation in the Raman analysis below.

C. Raman measurements

The Raman images of the spherical indentations were recorded with a custom confocal Raman microscope similar to that used previously^{3,13} operated with a 405 nm wavelength laser excitation. The linearly polarized [110] laser light was reflected from a longpass Raman edge filter and focused onto the sample using a 0.75 numerical aperture air objective. The laser power at the sample surface was set nominally at 1 mW. The information depth for the combination of the excitation and scattered light was approximately 80 nm.³ The scattered Raman signal was collected through the same objective and sent through a multimode fiber to a 1/2 m spectrograph equipped with a 2400 lines/mm grating and a charge-coupled device detector. The hyperspectral image was created by raster-scanning the sample through the focus using a closed-loop, (x, y) piezoelectric scanning stage and acquiring a spectrum at each spatial position (128 \times 128 pixels) with an integration time of 2 s/pixel over a total scan area of 50 $\mu\text{m} \times$ 50 μm (total collection time for each image was about 9 h; step size was \approx 0.394 μm). The Raman wave-number shifts (cm^{-1}) were calibrated using known atomic emission lines from Hg and Ar discharge lamps and a precise measure of the laser wavelength obtained from a wavemeter. The Si optical phonon line intensity at approximately 520.5 cm^{-1} was fit to a Pearson VII lineshape function using a conventional non-linear least squares algorithm. The peak position at a reference point far from the indentation (about 35 μm) was subtracted from the peak position at each pixel to arrive at a map of relative Raman peak shifts, $\Delta\nu(\text{cm}^{-1})$.

D. Raman predictions

In the absence of strain, diamond cubic Si exhibits three degenerate optical Raman modes (two transverse, one longitudinal) at an energy, ν_0 , of approximately 520.5 cm^{-1} .^{4,6,8} Under hydrostatic (equitriaxial or spherical) strain, the energies of the modes shift but remain degenerate. Under deviatoric strain, the degeneracy is lifted and the three modes

have separate energies, $\nu^{(\alpha)}$, and scattering intensities, $I^{(\alpha)}$, where α is the mode index. Usual Raman experimental conditions at room temperature do not separate the modes and the Raman spectrum around 520.5 cm^{-1} appears as a single shifted, broadened peak. For small strains (as in the elastic deformation here), the energy shifts for the three modes are also small and a predicted net single peak shift, $\Delta\nu_{\text{pre}}$, is given by the intensity-weighted sum of the shifts of the three modes

$$\Delta\nu_{\text{pre}} = \frac{\sum_{\alpha=1}^3 I^{(\alpha)} \Delta\nu^{(\alpha)}}{\sum_{\alpha=1}^3 I^{(\alpha)}},$$

where $\Delta\nu^{(\alpha)} = \nu^{(\alpha)} - \nu_0$ is the (α) mode shift. Importantly, both $\nu^{(\alpha)}$ and $I^{(\alpha)}$ are calculable from a tensor determinant that involves the Green strain tensor components, η_{ij} , and the cubic phonon deformation potentials, p , q , r , that characterize the change in material polarizability with strain. Details can be found elsewhere.^{4,6,8} To first approximation, a positive net shift is representative of a compressive (negative) strain field. (The Green finite strain tensor was used to retain consistency with the cited phonon deformation potentials^{28–30}—for the small distortions here, the infinitesimal strain tensor is almost identical.²⁷) The calculated strains were then used in the tensor determinant calculation to determine the predicted Raman shift at each point in the scan, $\Delta\nu_{\text{pre}}(x, y)$. Two sets of phonon deformation potentials, (p, q, r) ^{29,30} were used in the calculations giving almost identical shift results. Only results from the most recent set³⁰ are shown here. It should be clear that apart from the (limited) selection of (p, q, r) values, there are no adjustable parameters in the Raman shift predictions.

III. RESULTS

A. EBSD maps

Figure 2 shows color-filled contour maps of several of the strain components as determined by EBSD measurements in the strain field surrounding the indentation. The horizontal right direction $[1\bar{1}0]$ is x_1 and the vertical up direction $[110]$ is x_2 for all four maps. The length scale is the same in Figs. 2(a), 2(b), and 2(d); Fig. 2(c) shows the full $50 \mu\text{m}$ field at an expanded length scale (the wafer flat is below the bottom and parallel to the edge of the image). The gray discs approximate the size of the residual indentation impression; to avoid confusion with signals from plastically deformed and phase transformed material, data are not considered within these discs.^{18–20,22,23} The reference location (assumed zero strain) is at the edge of Fig. 2(c), consistent with the contour map. The color scale for strain is common to all the maps in Fig. 2.

It is clear from the contours that the normal strain fields ϵ_{11} and ϵ_{22} alternate maximum tension and compression along perpendicular $\langle 110 \rangle$ crystallographic directions consistent with previous two-fold EBSD and four-fold Raman observations.^{18,19,22,23} The shear strain field ϵ_{12} alternates directions of maximum intensity along perpendicular $\langle 100 \rangle$ crystallographic directions, also consistent with previous

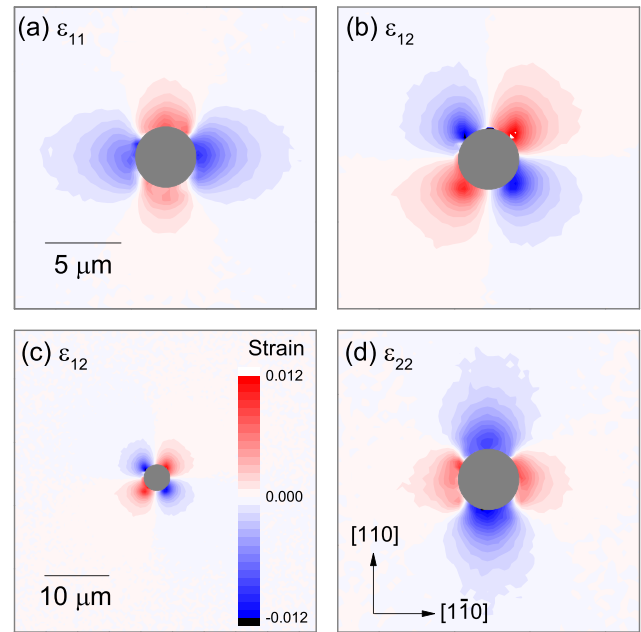


FIG. 2. Color-filled contour maps of EBSD-measured strain components (a) ϵ_{11} , (b) and (c) ϵ_{12} , and (d) ϵ_{22} adjacent to a spherical indentation impression (see Fig. 1) in Si. Measured by EBSD. x_1 and x_2 directions correspond to $[1\bar{1}0]$ and $[110]$, respectively. All strain components are dimensionless.

EBSD observations.^{22,23} It is also clear that the indentation strain field extends about three to four indentation diameters from the indentation, in accordance with the common “rule of thumb”³¹ and made most clear in Fig. 2(c). The strain components not shown (ϵ_{23} , ϵ_{13}) were all about an order of magnitude smaller than those shown in Fig. 2 and displayed weaker crystallographic dependences. The *entire* displacement gradient dataset, those components mapped in Fig. 2 and those not, formed the basis for predicting the Raman shift adjacent to the indentation.

B. Raman maps

Figure 3 shows color-filled contour maps of the relative Raman shifts $\Delta\nu(x, y)$ determined by confocal Raman microscopy measurements surrounding the indentation. The orientation and geometry are the same as in Fig. 2. Figure 3(b) shows the full $50 \mu\text{m}$ field. The reference location (assumed zero strain) is at the edge of Fig. 3(b), consistent with the strain maps, Fig. 2. The color scale for shift is common to both maps in Fig. 3.

In common with previous observations,^{19,20} the Raman shift exhibits four-fold symmetry through the appearance of lobes of positive shift aligned along $\langle 110 \rangle$ directions. There were two small regions of negative shift aligned along $\langle 100 \rangle$ directions (these latter were more obvious previously and the crystallography of slip leading to compensating lobes of tension and compression has been considered in some detail¹⁹). The shift field extends about three to four indentation diameters as in the EBSD observations above and made clear in Fig. 3(b).

C. Predicted Raman maps

Figure 4 shows color-filled contour maps of the relative Raman shifts $\Delta\nu_{\text{pre}}(x, y)$ predicted from EBSD strain

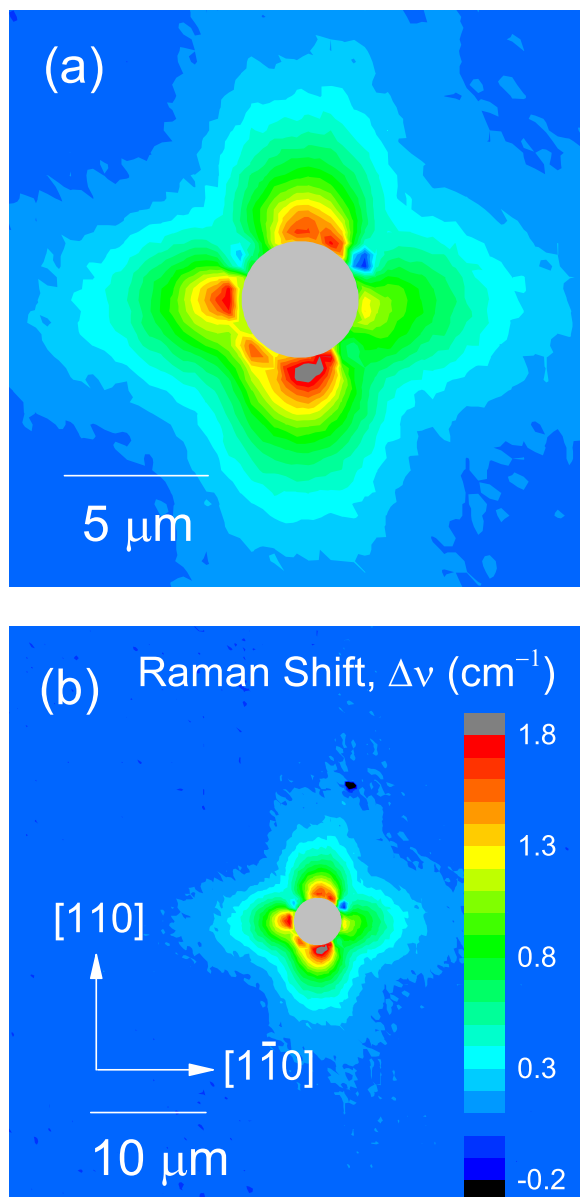


FIG. 3. Color-filled contour maps of measured Raman shift adjacent to a spherical indentation impression (see Fig. 1) in Si. Measured by Raman spectroscopy. Compare with Fig. 4.

measurements surrounding the indentation. The orientation and geometry are the same as in Figs. 2 and 3. Figure 4(b) shows the full 50 μm field. The color scale for shift is common to both maps in Fig. 4 and the same as Fig. 3.

Direct visual comparison of Figs. 3 and 4 shows the 2-D correlation between the measured and predicted Raman shifts to be strong: Most obvious is that the prediction exhibits four-fold symmetry in the form of {110} lobes of positive Raman shift as does the observation, the agreement extending to the observed characteristic magnitude, about 1.0 cm⁻¹. The prediction, Fig. 4, also exhibits small intervening regions of negative shift (shown as dark color) aligned along {100} in common with the observation, Fig. 3. As the strain field from which it is derived exhibits a length scale of about three to four indentation diameters (Fig. 2), so too does the predicted shift, in common with the observation.

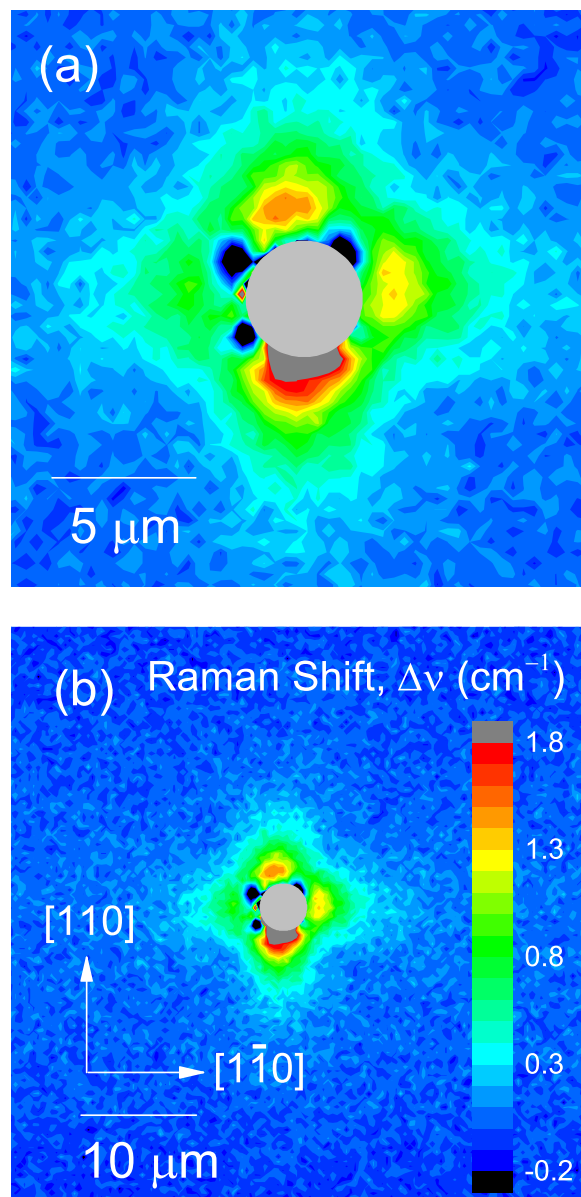


FIG. 4. Color-filled contour maps of Raman shift adjacent to a spherical indentation impression (see Fig. 1) in Si. Predicted by mechanical-spectroscopic analysis from EBSD measurements (Fig. 2). Compare with Fig. 3.

As before,²³ 1-D line scans extracted from the 2-D maps enable quantitative comparisons (remembering that there are no adjustable Raman shift parameters). Figure 5 shows 1-D line scans of measured and predicted shifts extending through the center of the indentation in the (a) vertical and (b) horizontal directions (scans aligned to within <0.2 μm of the apparent indentation center). Raman spectroscopy measurements are shown as the solid lines, EBSD-based predictions are shown as the open symbols, and the grey bars approximate the size of the residual indentation impression; data are not considered within these bars. As the center of the indentation was not known, the datasets were translated along the abscissa (about 1 μm) to obtain the best visual fit.

As with the maps, the 1-D scans of Fig. 5 show the correlation between the measured and predicted Raman shifts to be strong. Most obvious is that both datasets exhibit large

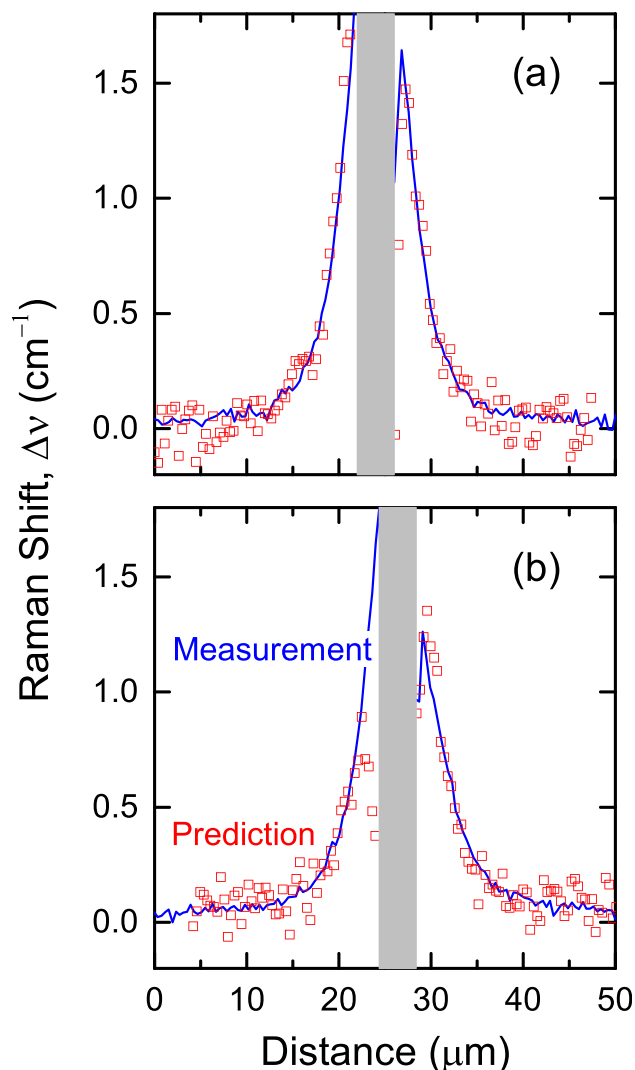


FIG. 5. Line scans comparing measured and predicted Raman shifts along traverses through a residual indentation impression (see Figs. 3 and 4); (a) vertical, along x_2 ; (b) horizontal, along x_1 .

increases in shift toward the center; both the magnitudes, about 1.5 cm^{-1} , and half-widths, about $5 \mu\text{m}$, of the increases are in common. Less obvious is that both measured and predicted shifts exhibit rapid decreases in shift adjacent to the impression (although there is some scatter).

IV. CONCLUSIONS

Figures 3, 4, and 5 make clear that the agreement between EBSD and Raman measurements of the effects of strain achieved in 1-D can be extended to 2-D. As before, the full strain tensor determination by EBSD can be manipulated into the scalar Raman shift for direct comparison of (Raman) measured and (EBSD) predicted responses,³ in this case in 2-D rather than 1-D. In the previous case of the 1-D wedge indentation, the agreement between the measured and predicted responses was very good remote from the indentation impression and less good adjacent to the impression. Here, line scans drawn from the 2-D spherical indentation show the agreement to be more uniform, although both comparisons show very good qualitative agreement (e.g., the rapid decreases in strain

adjacent to the impression) and quantitative agreement (e.g., the peak magnitudes of the shifts). In terms of identifying the full 2-D nature of strain fields in MEMS devices, this work shows both techniques to be applicable.

The small disagreements between the measured and predicted responses, particularly in Figs. 3–5, suggest where improvements in 2-D strain mapping can be made. First, background. The small disagreements between EBSD-predicted and measured Raman shifts demonstrated in these figures would have been worse without the 2-D linear background correction to the $A_{ij}(x, y)$ components. Without the background correction, disagreements in Figs. 3–5 would have reached 0.3 cm^{-1} . The need for the 2-D linear background correction may have been a consequence of “drift” during the long scan times required to generate a 2-D EBSD map as opposed to a 1-D line scan. Background correction can relatively easily be performed in 2-D ($4 \times 128 = 512$ points are needed), but requires knowledge of a reference deformation state in 2-D (here, zero deformation at the image periphery was used). (Raman measurements are less susceptible to this effect.) (Both EBSD and Raman measurements were initially conducted with $20 \mu\text{m} \times 20 \mu\text{m}$ square scans, yielding agreement as shown in Figs. 3, 4, and 5. Eventual use of $50 \mu\text{m} \times 50 \mu\text{m}$ square scans was made to ensure that the reference locations, far from the indentation, were indeed at zero deformation.) Second, centering. The wedge indentation exhibited a deeper impression, greater elastic uplift, and presented fewer alignment issues. As a consequence, the edges and center of the impression were relatively easy to measure (by AFM) and the indentation strain field relatively easy to model (by FEA). Both features enabled the center of the indentation to be better estimated, and hence the measured and predicted responses better compared. Although, as noted in the Introduction, the EBSD and Raman measurements are already completely separate (“orthogonal”), the addition of the independent AFM and FEA further strengthens the assessment of accuracy. The incorporation of AFM and FEA into the 2-D measurement scheme is a clear next step. Third, and final, calibration. EBSD- and Raman spectroscopy-based assessments of strain depend on completely different physical phenomena. EBSD measurements derive from elastic scattering of electrons from fixed atoms and Raman measurements derive from inelastic scattering of photons from vibrating atoms. An independent strain standard¹⁵ is thus required to converge the two measurement techniques, preferably a standard that enables the Raman measurement to be calibrated under multiaxial strain conditions, similar to those measured here.

ACKNOWLEDGMENTS

This research was performed while A.J.G. was a member of the NIST Summer Undergraduate Research Fellowship (SURF) program. Certain commercial equipment, instruments, or materials are identified in this document. Such identification does not imply recommendation or endorsement by the National Institute of Standards and Technology, nor does it imply that the products identified are necessarily the best available for the purpose.

- ¹F. W. DelRio, R. F. Cook, and B. L. Boyce, *Appl. Phys. Rev.* **2**, 021303 (2015).
- ²M. D. Vaudin, Y. B. Gerbig, S. J. Stranick, and R. F. Cook, *Appl. Phys. Lett.* **93**, 193116 (2008).
- ³L. H. Friedman, M. D. Vaudin, S. J. Stranick, G. Stan, Y. B. Gerbig, W. A. Osborn, and R. F. Cook, *Ultramicroscopy* **163**, 75 (2016).
- ⁴Q. Ma, S. Chiras, D. R. Clarke, and Z. Suo, *J. Appl. Phys.* **78**, 1614 (1995).
- ⁵V. Senez, A. Armigliato, I. De Wolf, G. Carnevale, R. Balboni, S. Frabboni, and A. Benedetti, *J. Appl. Phys.* **94**, 5574 (2003).
- ⁶R. P. Koseski, W. A. Osborn, S. J. Stranick, F. W. DelRio, M. D. Vaudin, T. Dao, V. H. Adams, and R. F. Cook, *J. Appl. Phys.* **110**, 073517 (2011).
- ⁷G. A. Myers, S. S. Hazra, M. P. de Boer, C. A. Michaels, S. J. Stranick, R. P. Koseski, R. F. Cook, and F. W. DelRio, *Appl. Phys. Lett.* **104**, 191908 (2014).
- ⁸I. De Wolf, J. Vanhellemont, A. Romano-Rodriguez, H. Norstrom, and H. E. Maes, *J. Appl. Phys.* **71**, 898 (1992).
- ⁹I. De Wolf, H. E. Maes, and S. K. Jones, *J. Appl. Phys.* **79**, 7148 (1996).
- ¹⁰J. He, M. C. Shaw, N. Sridhar, B. N. Cox, and D. R. Clarke, in *Electronic Packaging Materials Science X*, edited by D. J. Belton, M. Gaynes, E. G. Jacobs, R. Pearson, and T. Wu (Materials Research Society, Pittsburgh, PA, 1998), pp. 99–104.
- ¹¹A. J. Wilkinson, *Appl. Phys. Lett.* **89**, 241910 (2006).
- ¹²S. Villert, C. Maurice, C. Wyon, and R. Fortunier, *J. Microsc.* **233**, 290 (2009).
- ¹³M. D. Vaudin, G. Stan, Y. B. Gerbig, and R. F. Cook, *Ultramicroscopy* **111**, 1206 (2011).
- ¹⁴J. A. Howell, M. D. Vaudin, and R. F. Cook, *J. Mater. Sci.* **49**, 2213 (2014).
- ¹⁵M. D. Vaudin, W. A. Osborn, L. H. Friedman, J. M. Gorham, V. Vartanian, and R. F. Cook, *Ultramicroscopy* **148**, 94 (2015).
- ¹⁶E. Bonera, M. Fanciulli, and D. N. Batchelder, *J. Appl. Phys.* **94**, 2729 (2003).
- ¹⁷U. Schmidt, W. Ibach, K. Müller, K. Weishaupt, and O. Hollricher, *Vib. Spectrosc.* **42**, 93 (2006).
- ¹⁸Y. B. Gerbig, S. J. Stranick, D. J. Morris, M. D. Vaudin, and R. F. Cook, *J. Mater. Res.* **24**, 1172 (2009).
- ¹⁹Y. B. Gerbig, S. J. Stranick, and R. F. Cook, *Scr. Mater.* **63**, 512 (2010).
- ²⁰Y. B. Gerbig, S. J. Stranick, and R. F. Cook, *Phys. Rev. B* **83**, 205209 (2011).
- ²¹A. J. Wilkinson, G. Meaden, and D. J. Dingley, *Superlattices Microstruct.* **45**, 285 (2009).
- ²²A. J. Wilkinson and T. B. Britton, *Mater. Today* **15**, 366 (2012).
- ²³T. B. Britton, J. Jiang, R. Clough, E. Tarleton, A. I. Kirkland, and A. J. Wilkinson, *Ultramicroscopy* **135**, 136 (2013).
- ²⁴V. Domnich, Y. Gogotsi, and S. Dub, *Appl. Phys. Lett.* **76**, 2214 (2000).
- ²⁵T. Juliano, V. Domnich, and Y. Gogotsi, *J. Mater. Res.* **19**, 3099 (2004).
- ²⁶A. J. Wilkinson, G. Meaden, and D. J. Dingley, *Ultramicroscopy* **106**, 307 (2006).
- ²⁷G. E. Mase, *Continuum Mechanics* (McGraw-Hill, New York, 1970).
- ²⁸S. Ganesan, A. A. Maradudin, and J. Oitmaa, *Ann. Phys.* **56**, 556 (1970).
- ²⁹E. Anastassakis, A. Pinczuk, and E. Burstein, *Solid State Commun.* **8**, 133 (1970).
- ³⁰E. Anastassakis, A. Cantarero, and M. Cardona, *Phys. Rev. B* **41**, 7529 (1990).
- ³¹K. L. Johnson, *Contact Mechanics* (Cambridge University Press, Cambridge, United Kingdom, 1996).